Kiala *et al. Discover Water* (2026) 6:41
https://doi.org/10.1007/s43832-026-00360-z

Discover Water

RESEARCH

Open Access

Operational sentinel-2 system for monthly near-real-time irrigated area mapping in the Limpopo river basin

Zolo Kiala[1*], Karthikeyan Matheswaran[2], Chris Dickens[2], Mariangel Garcia Andarcia[2], Fulco Ludwig[2] and Surajit Ghosh[2]

*Correspondence:
Zolo Kiala
Z.Kiala@cgiar.org
[1]International Water Management Institute, Block G Ground Floor, Hatfield Gardens, 333 Grosvenor St, Hatfield, 0083 Pretoria, South Africa
[2]International Water Management Institute, 127 Sunil Mawatha, Battaramulla 10120, Sri Lanka

Abstract
Monitoring irrigated agriculture is critical in the water-scarce Limpopo River Basin (LRB). However, existing approaches are often coarse, retrospective, or season-aggregated, which limits their ability to capture smallholder irrigation and the month-to-month dynamics required for operational management. This study addresses this gap by developing and validating a scalable, semi-supervised framework to produce monthly dry-season (May–September) 10 m irrigated-area maps and associated water-use estimates across the LRB for 2019–2024. The workflow integrates Sentinel-2 imagery, a Random Forest classifier, time-lagged precipitation–vegetation analysis, and slope masking in Google Earth Engine, and links mapped irrigated area to FAO's WaPOR (Water Productivity through Open access of Remotely sensed derived data) evapotranspiration to estimate water use. Validation against independent field observations ($n = 190$) achieved 80% overall accuracy ($\kappa = 0.60$). Dry-season irrigated area declined from ~211,000 ha (2019) to ~185,000 ha (2024), while mean dry-season water use increased from ~103–134 × 10^6 m^3, indicating rising irrigation intensity. Irrigation hotspots were concentrated in key sub-basins including the Middle Olifants, Crocodile, and Letaba. The resulting open-access, basin-scale product provides operational irrigation intelligence to support transboundary water allocation and drought response. It also offers a replicable model for other water-stressed basins.

Keywords Digital twin, Irrigated agriculture, Random forest, Sentinel-2, WaPOR

1 Introduction

Irrigated agriculture accounts for approximately 70% of global freshwater withdrawals and is a critical pillar of food security and rural livelihoods [32]. The challenges associated with irrigation are particularly acute in water-scarce basins, where population growth, dietary shifts, and climate variability are driving increased pressure on limited water resources. The Limpopo River Basin (LRB) is one of Southern Africa's major transboundary river systems, supporting approximately 18 million predominantly rural inhabitants. The basin experiences severe water stress characterized by prolonged dry spells, declining baseflows, and rising temperatures [8, 39]. Irrigation plays a central role in agricultural production and employment; however, between 2000 and 2012, annual irrigation water consumption more than doubled, from approximately 1,400 to $3{,}000 \times 10^6$ m^3, placing additional strain on already over-allocated sub-basins [18].

Agricultural systems in the LRB are highly heterogeneous, encompassing large-scale commercial farms, formal and informal smallholder irrigation schemes, and widespread subsistence agriculture. In this context, near-real-time irrigation monitoring is essential to understand where and when irrigation occurs and how much water is used [22]. Such information is critical for seasonal water allocation, drought response, and adaptive basin management. However, most existing irrigation assessments in the region are based on historical or seasonally aggregated analyses, limiting their relevance for in-season decision-making [23, 37]. In addition, many conventional approaches rely on extensive field data collection during the irrigation season, constraining their scalability and operational deployment across large transboundary basins [40].

Remote sensing has been widely used to map irrigated agriculture, with early studies relying on coarse- to medium-resolution sensors such as AVHRR, MODIS, and Landsat to distinguish irrigated from rainfed systems using vegetation indices and seasonal phenology [27, 31, 40]. While effective for large-scale assessments, these approaches perform poorly in heterogeneous agricultural landscapes. In sub-Saharan Africa, where smallholder plots often measure less than one hectare, spatial resolutions coarser than 250 m systematically underestimate irrigated area due to mixed-pixel effects [40]. The advent of higher-resolution sensors, such as SPOT and Sentinel-2, has improved the detection of irrigated fields by enabling finer discrimination of crop phenology and water-use dynamics [22, 42, 45]. Nevertheless, major challenges persist, including fragmented fields, intra-seasonal variability, and informal irrigation practices, which continue to limit accurate and timely detection in many African contexts. These challenges underscore the need for operational systems that combine high spatial and temporal resolution imagery with robust classification frameworks to deliver actionable irrigation intelligence.

Within the LRB, prior remote-sensing studies have advanced understanding of irrigation patterns but remain constrained in their operational applicability. Van Niekerk et al. [41] estimated evapotranspiration at approximately 250 m resolution using Landsat-based datasets, which was suitable for regional water accounting but too coarse to resolve fragmented smallholder irrigation or support sub-basin allocation decisions. Cai et al. [5] mapped irrigated areas in South Africa's Limpopo Province using Landsat imagery and vegetation indices, demonstrating moderate classification performance but relying on static or seasonal representations that did not capture monthly dynamics. More recent Sentinel-2–based studies have improved spatial resolution (e.g., [28]), yet they have generally focused on irrigated-area classification alone, without explicitly linking mapped extents to quantified consumptive water use. As a result, these approaches provide limited support for near-real-time allocation and demand management in a highly dynamic, water-scarce basin.

Recent advances in cloud-based geospatial platforms now offer new opportunities to address these limitations. Google Earth Engine (GEE) enables basin-scale, high-resolution, and temporally consistent processing of satellite imagery [15], while FAO's WaPOR platform provides analysis-ready evapotranspiration products at 100 m resolution to support water-use assessments across Africa [9]. Despite the availability of these resources, the LRB still lacks an operational monitoring system capable of producing monthly, high-resolution irrigated-area maps and directly linking them to quantified water use for allocation planning. In this study, the methodological contribution does not lie in introducing a new algorithm, but rather in the operational integration of existing data sources and methods into a single, automated framework.

Building on this operational gap, we develop and validate a semi-supervised machine-learning framework for the LRB. The framework produces monthly 10 m irrigated-area maps and dry-season water-use estimates for the period 2019–2024. It integrates Sentinel-2 imagery with Random Forest classification and slope-based masking. Time-lagged precipitation–vegetation relationships are used to suppress rainfall-driven greenness responses. WaPOR evapotranspiration data are used to link irrigated area with consumptive water use. Unlike many previous studies, the system operates at monthly temporal resolution and is designed to capture fragmented smallholder irrigation at field scale. Irrigated-area mapping and water-use estimation are combined within a single automated workflow. The framework is implemented within the Limpopo Basin Digital Twin initiative (https://limpopo.digitaltwins.iwmi.org/). It minimizes reliance on in-seas on field data and supports reproducible, scalable, and operational irrigation monitoring in a water-stressed transboundary basin.

2 Materials and methods

2.1 Study area

The Limpopo River Basin (LRB), located between latitudes 22°S–26°S and longitudes 26°E–35°E, is the fourth-largest transboundary river basin in Southern Africa, draining approximately 416,300 km^2 across Botswana (19%), Zimbabwe (15%), South Africa (45%), and Mozambique (21%) [21] (Fig. 1). The basin spans a wide range of agro-climatic zones that strongly influence irrigation practices and remote-sensing classification performance. Mean annual precipitation is approximately 530 mm, decreasing westward to arid regions receiving ~ 200 mm yr^{-1} and increasing eastward and southward to semi-arid and sub-humid zones with rainfall locally exceeding 1,200–1,500 mm yr^{-1} [8, 39]. Rainfall is highly seasonal, concentrated in the wet season from October to April, while the dry season (May–September) is characterized by minimal precipitation (< 20 mm month^{-1}), during which irrigation becomes essential for crop production [21] (Fig. 2).

Topography varies from low-relief floodplains in Mozambique to higher-elevation plateaus and escarpments in South Africa and Zimbabwe, with a mean basin elevation of approximately 840 m. These gradients influence crop calendars, water availability, and the spectral separability between irrigated and rainfed systems [39]. Soils are predominantly sandy to sandy loam with low water-holding capacity across much of the basin, particularly in western and northern regions, while heavier loams and clays occur in floodplain areas of Mozambique [21]. Such soil properties increase crop sensitivity to water stress and enhance vegetation contrast between irrigated and non-irrigated fields during the dry season.

Hydrologically, irrigation in the LRB is supported by a combination of regulated surface-water systems, including major tributaries such as the Crocodile, Olifants, and Limpopo main stem, large reservoir schemes, and widespread groundwater abstraction, particularly in smallholder and informal irrigation systems [18, 39]. Groundwater use

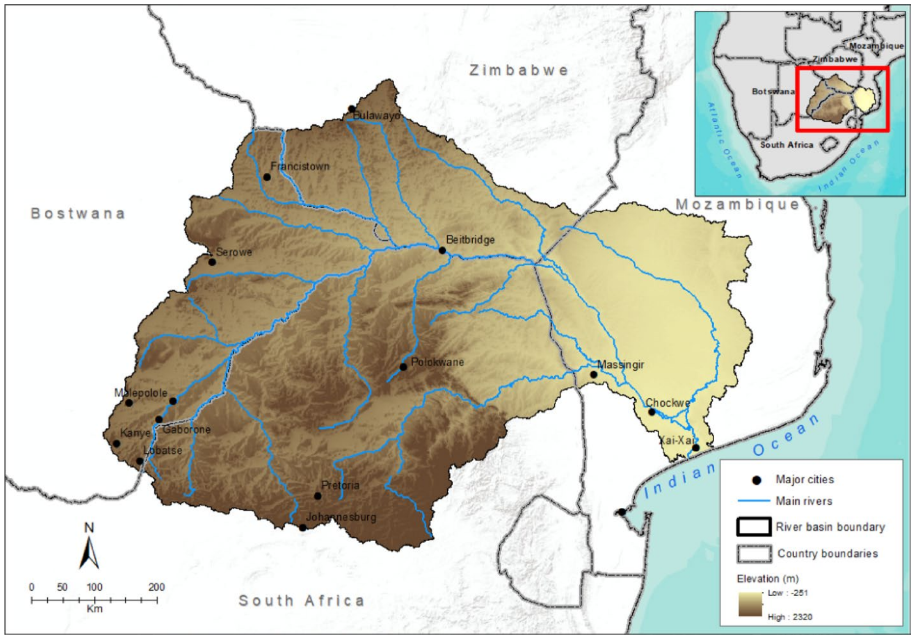

Fig. 1 Map of the Limpopo River Basin showing basin boundaries, major rivers (Limpopo in blue), and key urban centres. Elevation is derived from the Copernicus GLO-30 Digital Elevation Model (DEM) (2021). Basin and river boundaries were sourced from the Limpopo Watercourse Commission (LIMCOM) and HydroSHEDS [19], and country boundaries were obtained from FAO's Global Administrative Unit Layers (GAUL) dataset [11]. All spatial data are displayed in the WGS 84 geographic coordinate reference system (EPSG:4326)

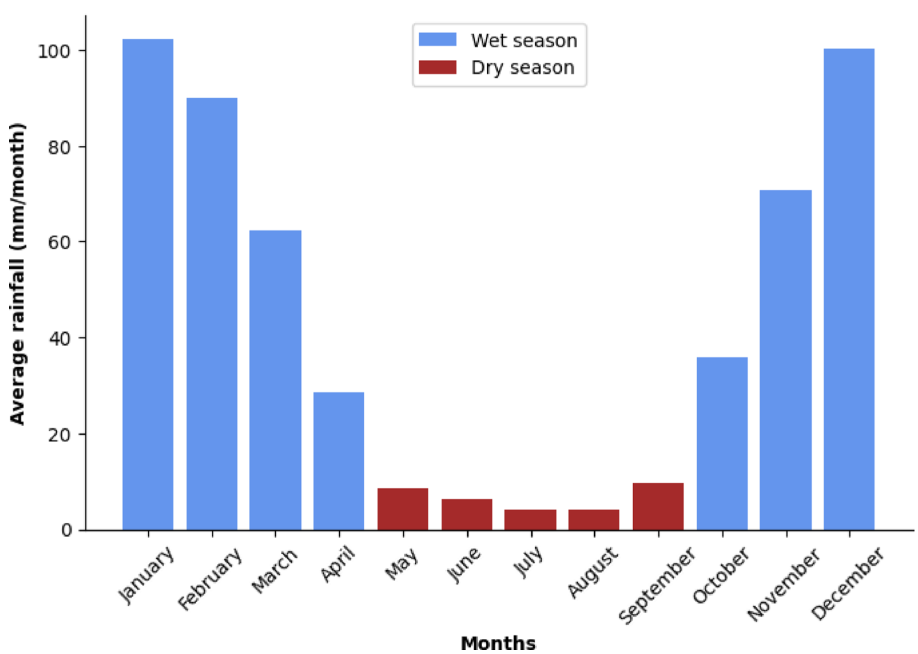

Fig. 2 Long-term (1981–2024) mean monthly rainfall in the LRB computed from CHIRPS data. Blue bars represent the wet season (October–April) and red bars denote the dry season (May–September)

is especially prevalent in fractured rock aquifers associated with the Bushveld Igneous Complex and alluvial aquifers along river corridors [21]. This diversity of water sources contributes to pronounced spatial heterogeneity in irrigation patterns, posing challenges for classification but underscoring the need for high-resolution, temporally resolved monitoring.

Together, the basin's strong climatic gradients, heterogeneous soils, and mixed surface- and groundwater-based irrigation systems provide a robust test environment for evaluating operational irrigated-area mapping approaches in water-scarce, transboundary settings.

2.2 Methodology

2.2.1 Input datasets

This study presents a fully automated, semi-supervised approach for mapping irrigated areas in the Limpopo River Basin (LRB), implemented in Google Earth Engine (GEE) and applied for each dry-season month (May–September) from 2019 to 2024. Sentinel-2 Level-2 A surface reflectance imagery was used as the primary dataset for irrigated-area classification. Cropland extent was defined using cropland boundaries from the Department of Agriculture, Land Reform and Rural Development (DALRRD; April 2017 release) refined with the 2022 South African National Land Cover (SANLC) dataset (see Supplementary Table) for South Africa, and the ESA WorldCover 10 m product (2021) for Botswana, Mozambique, and Zimbabwe [43]. Precipitation inputs were obtained from the Climate Hazards Group InfraRed Precipitation with Stations (CHIRPS) dataset [12], and vegetation dynamics used in time-lag analysis were derived from Landsat-8 NDVI. Terrain constraints were represented using slope derived from the Copernicus GLO-30 Digital Elevation Model. Irrigation water use was quantified using FAO WaPOR v3 Level 2 monthly Actual Evapotranspiration and Interception (AETI) data. Independent validation data comprised field observations collected in 2024 and visually interpreted PlanetScope imagery.

An interactive web application implementing the workflow is available at https://huggingface.co/spaces/IWMIHQ/irrigated-agriculture-extractor, supporting replication and adaptation to other basins with similar conditions.

2.2.2 Preprocessing

A basin-wide cropland mask was generated to constrain irrigation mapping to likely agricultural land. For South Africa, DALRRD cropland boundaries were refined using SANLC 2022 field extents (see Supplementary Table). For Botswana, Mozambique, and Zimbabwe, cropland areas were derived from ESA WorldCover 10 m [43] and quality-checked using visual interpretation of 100 randomly selected points against high-resolution Google Earth imagery. Because these products do not explicitly represent cropland expansion or abandonment during 2019–2024, the merged cropland layer was used strictly as a static spatial mask to define the analysis domain.

Sentinel-2 imagery was filtered to retain scenes with CLOUDY_PIXEL_PERCENTAGE < 10%, and cloud/cloud-shadow pixels were masked using the Sentinel-2 Scene Classification Layer (SCL) (excluding SCL = 3 and SCL = 7–9). Monthly median composites were then generated within the cropland mask to reduce atmospheric variability and residual contamination.

2.2.3 Feature generation

From monthly Sentinel-2 median composites, model features included raw spectral bands (B2, B3, B4, B5, B6, B7, B8, B8A, B11, and B12) and derived indices (NDVI (Normalized Difference Vegetation Index), Normalized Difference Built-up Index (NDBI), Green Index (GI), Green Chlorophyll Vegetation Index (GCVI), Land Surface Water Index (LSWI), Enhanced Vegetation Index (EVI), and Bare Soil Index (BSI). This feature set therefore included both greenness- and moisture-sensitive information. We also computed an irrigation-sensitive Normalized Green Index (NGI) as the product of NDVI and the Green Index (GI) [35]:

$$NGI = NDVI \times GI \tag{1}$$

NGI captures vegetation vigor by combining canopy density (NDVI) and greenness response (GI). Unlike single indices such as Soil-Adjusted Vegetation Index (SAVI) or Green Normalized Difference Vegetation Index (GNDVI), it emphasizes pixels that are high in both properties at the same time. This is useful in the dry season, when irrigation maintains greenness and non-irrigated crops typically senesce. For this reason, NGI was prioritized for semi-supervised training-sample selection rather than as an exclusive classification feature. Indices such as Normalized Difference Moisture Index (NDMI) or soil-adjusted variants may respond to surface moisture at early phenological stages, but this signal can remain weak or ambiguous before sustained canopy development [13, 14, 44]. The use of NGI therefore reflects a deliberate focus on high-confidence dry-season irrigation signals to reduce false positives at basin scale [16, 35].

2.2.4 Training data Preparation (semi-supervised reference data)

Semi-supervised reference data were derived from NGI using percentile thresholds within the cropland mask. To reduce mixed pixels and labeling uncertainty, candidate training samples were drawn from the distribution tails: pixels in the upper 10th percentile of NGI values were treated as irrigated candidates, while pixels in the lower 10th percentile were treated as non-irrigated candidates. This is consistent with the assumption that high dry-season vegetation vigour is largely sustained by irrigation [5].

In GEE, percentile-based class masks were generated using percentileReducer and reduceRegion, polygonized, and sampled using a stratified design (100 polygons per class; 200 samples per month). Sentinel-2 spectral band values and derived vegetation indices were extracted at each sample location to build the feature table used for model fitting (Fig. 3). This semi-supervised procedure reduces reliance on in-season field data and supports scalable, repeatable training-sample generation for near-real-time irrigation mapping.

This semi-supervised approach eliminates the need for extensive in-season field data while enabling scalable and repeatable generation of training samples for near-real-time irrigation mapping.

2.2.5 Model training and classification

A Random Forest (RF) classifier was trained using the extracted feature dataset [4]. Both raw Sentinel-2 spectral bands and multiple vegetation indices were included to capture complementary information on surface reflectance, vegetation structure, and moisture status across crop types and phenological stages. Although several indices are derived

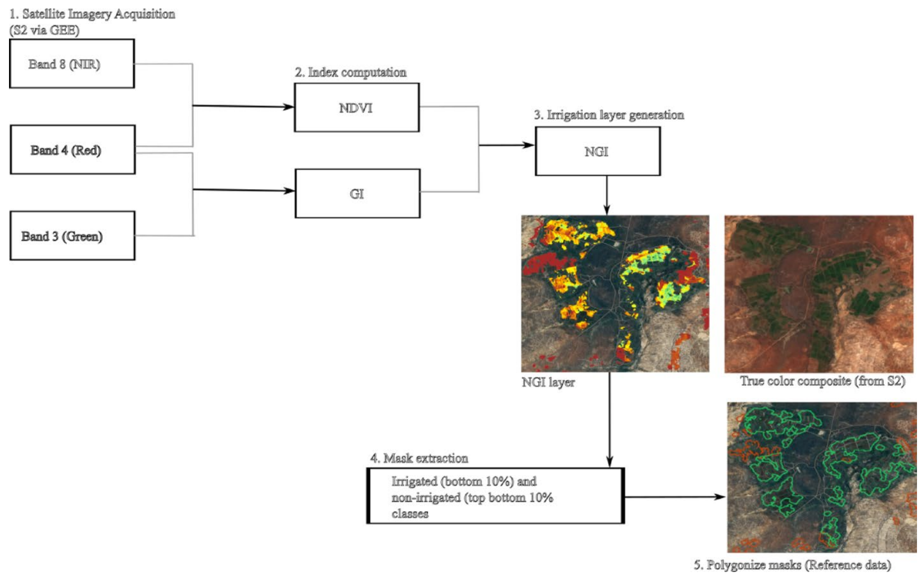

Fig. 3 Workflow for generating reference data from the Normalized Green Index (NGI)

from the same bands and are therefore partially collinear, RF is generally robust to multicollinearity because splits are selected across many trees using random subsets of predictors; correlated variables may reduce interpretability of individual predictors but typically do not degrade classification performance. Given the objective of accurate and repeatable mapping, no explicit feature selection or dimensionality reduction (e.g., PCA or VIF filtering) was applied.

Although NGI percentile thresholds were used only to define high-confidence irrigated and non-irrigated candidate samples, classification was performed using the full feature set. This enables the model to learn decision boundaries across the multidimensional spectral space and capture subtler differences beyond the NGI sampling tails. The RF model was implemented in GEE using ee.Classifier.smileRandomForest, configured with 100 trees and a fixed random seed of 42 to ensure reproducibility; all other hyperparameters were left at their library defaults to reduce tuning complexity and support consistent replication. As an ensemble method, RF also helps limit overfitting by averaging predictions across many decorrelated trees.

The trained model produced monthly binary irrigation classifications (irrigated/non-irrigated) and corresponding class-probability outputs at 10 m spatial resolution for each dry-season month. The overall classification workflow is summarized in Fig. 4.

2.2.6 Post-classification refinement

To reduce false positives and improve irrigation map reliability, two refinement steps were applied: time-lagged precipitation–vegetation filtering and slope masking.

Time-lagged regression A cross-correlation function (CCF) approach [3] was used to evaluate the lagged response of vegetation (Landsat-8 NDVI) to precipitation (CHIRPS) at 16-day intervals. Pixels with a positive correlation coefficient ($r > 0.35$) were interpreted as rainfall-driven (rainfed) and removed from the irrigated class. The threshold was determined empirically via sensitivity trials to balance omission and commission errors (see Fig. 5).

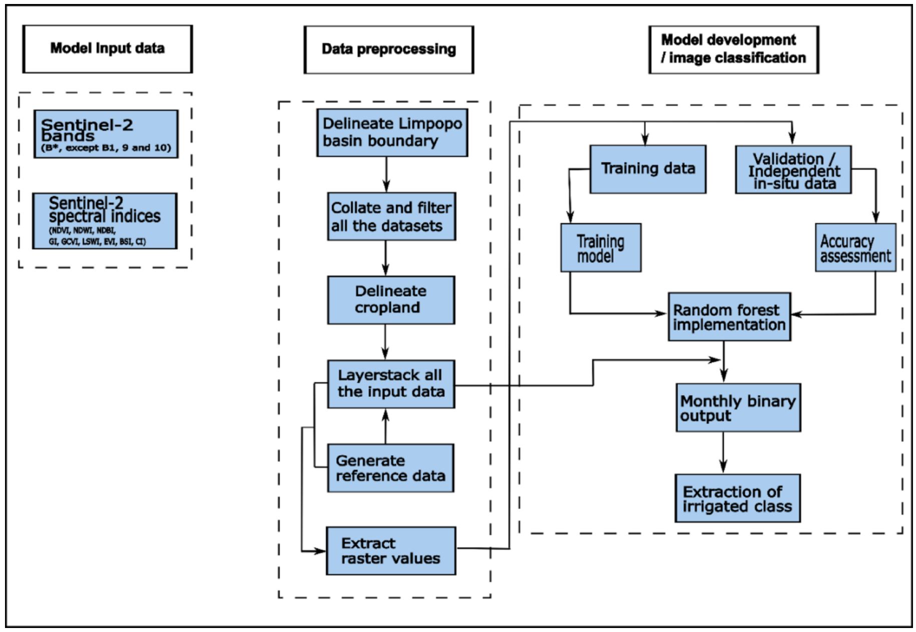

Fig. 4 Workflow for mapping irrigated areas using Sentinel-2 bands and indices, Random Forest classification, and in-situ accuracy assessment

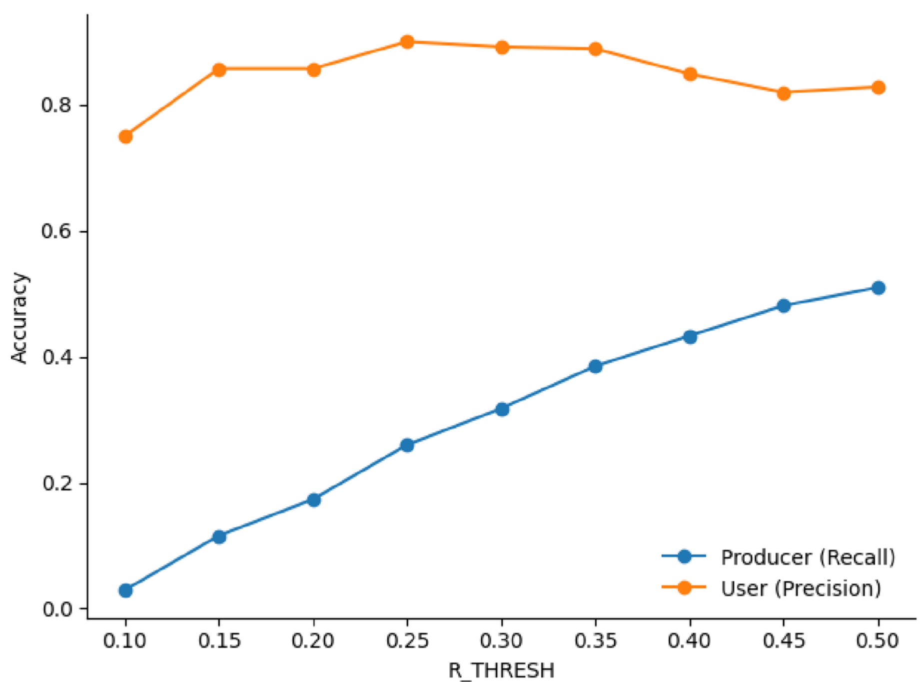

Fig. 5 Sensitivity of irrigated-class accuracy to the correlation threshold (r). Producer's accuracy (recall) increases steadily with higher thresholds, indicating reduced omission of irrigated pixels, while user's accuracy (precision) peaks around $r \approx 0.25$–0.35 and declines slightly thereafter, reflecting a trade-off between omission and commission errors. The selected threshold balances these two metrics to optimize irrigated mapping quality

Slope masking Areas with slopes > 5° were excluded based on irrigation feasibility constraints [36]. In the LRB, irrigated agriculture is predominantly located on low-gradient plains and valley bottoms, and field validation and visually interpreted samples did not indicate irrigation on slopes exceeding 5°, suggesting negligible omission from slope masking. Slope (degrees) was derived from the Copernicus GLO-30 DEM.

2.2.7 Validation

Model performance was evaluated using a holdout validation strategy based on independent reference data, rather than k-fold cross-validation. Three complementary validation approaches were applied: (i) independent in-situ field observations collected during the late dry season (30 September–5 October 2024) in Limpopo Province, South Africa; (ii) internal testing datasets held out from the training process for quantitative accuracy assessment; and (iii) qualitative comparison of mapped irrigated areas with known irrigation scheme locations.

Field observations were collected for 120 agricultural plots using the KoboToolbox mobile data collection platform. For each plot, irrigation status (irrigated/non-irrigated), irrigation type, dominant crop type, and primary water source were recorded, and locations were captured using GPS-enabled devices. Representative field photographs illustrating non-irrigated and irrigated conditions are shown in Fig. 6.

To supplement field observations and improve spatial coverage across irrigation system types, an additional 70 reference samples were derived through visual interpretation of high-resolution PlanetScope imagery (4.77 m) accessed via GEE. These samples were selected within known irrigation schemes (see Supplementary Table) and classified based on field geometry, vegetation condition during the dry season, and visible irrigation infrastructure.

All validation samples were used exclusively for accuracy assessment and were not incorporated into model training. When combined, field-based and PlanetScope-derived

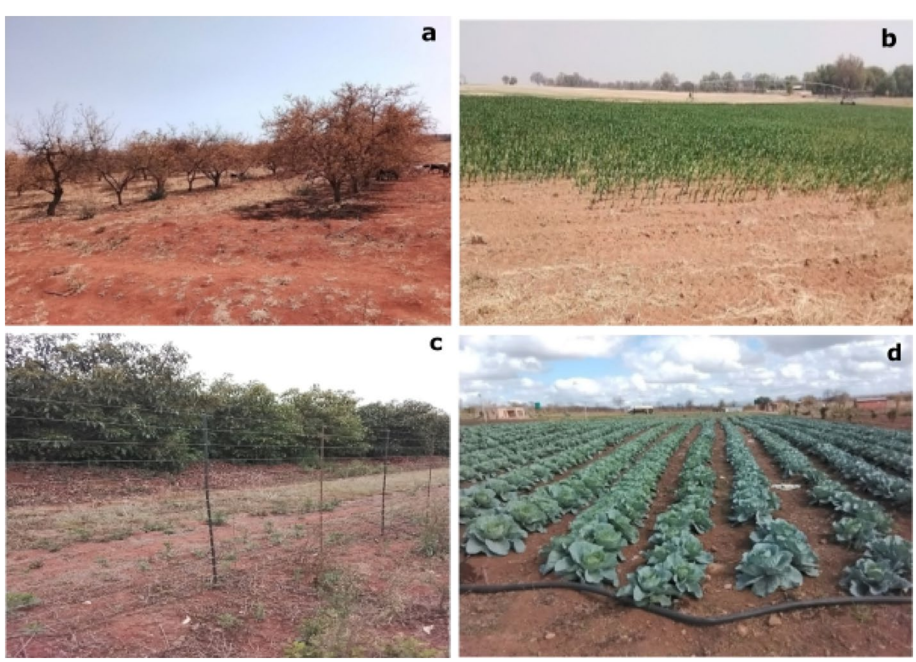

Fig. 6 Field observation photographs of non-irrigated (a, c) and irrigated crops (b, d)

samples produced a near-balanced validation dataset of 190 reference points (98 non-irrigated, 92 irrigated). Classification performance was quantified using confusion matrices and standard accuracy metrics, including overall accuracy, producer's and user's accuracies, F-scores, and Cohen's Kappa. The spatial distribution of surveyed irrigated fields is shown in Fig. 7.

Field validation data were more densely available in South Africa than in other parts of the Limpopo River Basin, reflecting differences in data availability rather than methodological bias. Cropping systems, irrigation practices, and field sizes vary across the basin, particularly in Botswana, Zimbabwe, and Mozambique, where irrigation is often more fragmented and informal. Although consistent decision thresholds and post-classification filters were applied basin-wide to support operational deployment, classification performance may vary locally. Reported accuracy metrics should therefore be interpreted as representative of basin-scale performance, rather than as country-specific accuracy estimates.

To strengthen confidence in areas with limited field data, a supplementary qualitative assessment was conducted in underrepresented regions. High-resolution satellite imagery available through Google Earth and PlanetScope was examined to evaluate the spatial plausibility of mapped irrigated areas, with attention to dry-season persistence of greenness, field patterns, proximity to water sources, and visible irrigation features. While this assessment does not provide quantitative accuracy measures, it supports the broader spatial consistency of mapped irrigation patterns beyond South Africa and highlights localized uncertainties in fragmented or mixed-use agricultural landscapes. Representative examples are provided in the Data Availability materials.

2.2.8 Estimation of irrigation water use

Irrigation water use was quantified using FAO WaPOR v3 Level 2 monthly AETI (100 m). To integrate AETI with the 10 m irrigated-area maps, WaPOR data were

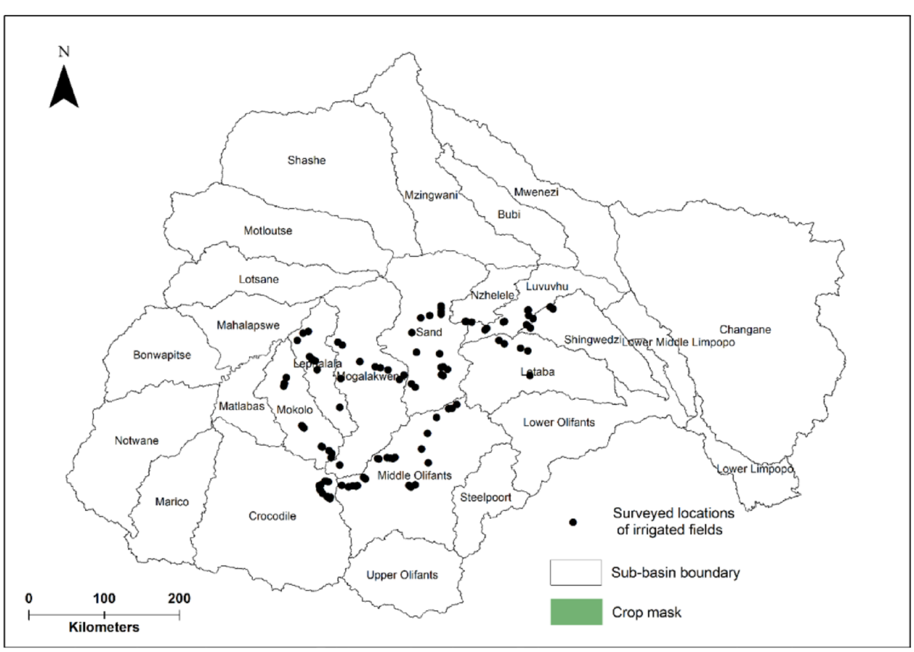

Fig. 7 Locations of surveyed irrigated fields

resampled using nearest-neighbour interpolation, preserving original pixel values and thus maintaining the physical integrity of WaPOR measurements [20]. Nearest-neighbour resampling has also been used in WaPOR-based studies in the LRB where coarser WaPOR products were integrated with finer spatial grids without altering evapotranspiration values [7].

The classified irrigated raster was converted to polygons, and mean AETI values (mm month^{-1}) were extracted per polygon using zonal statistics. WaPOR Level 2 AETI values are provided as digital numbers (DN) with a scale factor of 0.1, converted as:

$$AETI_{mm} = DN \times 0.1 \tag{2}$$

$$V\,(m3) = (AETI_{mm}/1000) \times A \tag{3}$$

where A is polygon area (m^2). Total irrigation water use was obtained by aggregating volumes across irrigated polygons.

2.2.9 Statistical analysis

All statistical analyses were performed in Python 3.x using SciPy, with statsmodels used for Tukey's HSD where applicable. For parametric tests (ANOVA and t-tests), assumptions of approximately normal residuals and homogeneity of variance were evaluated using residual diagnostics, Shapiro–Wilk tests for normality, and Levene's tests for equality of variances. When these assumptions were not met, data were $\log_{10}$-transformed prior to analysis; results are reported in the original units for interpretability.

Interannual differences in irrigated area were tested using one-way ANOVA, treating years as groups and using dry-season months (May–September) as within-year replicates. Seasonal (monthly) differences were tested by treating months as groups with years as replicates. When ANOVA indicated a significant effect, Tukey's HSD was applied for post-hoc pairwise comparisons to control the family-wise error rate. Targeted comparisons between specific months (e.g., May vs. August and May vs. September) were assessed using paired t-tests (paired by year), because month-to-month values represent repeated measures within the same year and study domain.

Classification bias was evaluated using McNemar's χ^2 test, which assesses whether misclassification errors are symmetric between irrigated and non-irrigated classes, complementing overall accuracy and Cohen's kappa. Spatial clustering of irrigated area across sub-basins was assessed using Global Moran's I, where positive values indicate that similar values are spatially clustered rather than randomly distributed. All tests used a significance level of $\alpha = 0.05$, and test statistics, degrees of freedom (where applicable), and p-values are reported.

2.3 Results

2.3.1 Cropland extent

The composite cropland mask for the LRB covered 4.37×10^6 ha (9.5% of the basin), with South Africa accounting for 3.02×10^6 ha (~70%). The remainder was in Botswana (0.59×10^6 ha), Zimbabwe (0.53×10^6 ha), and Mozambique (0.24×10^6 ha) (Fig. 8). The mask, encompassing both rainfed and irrigated areas, formed the baseline for near-real-time monthly irrigated area mapping.

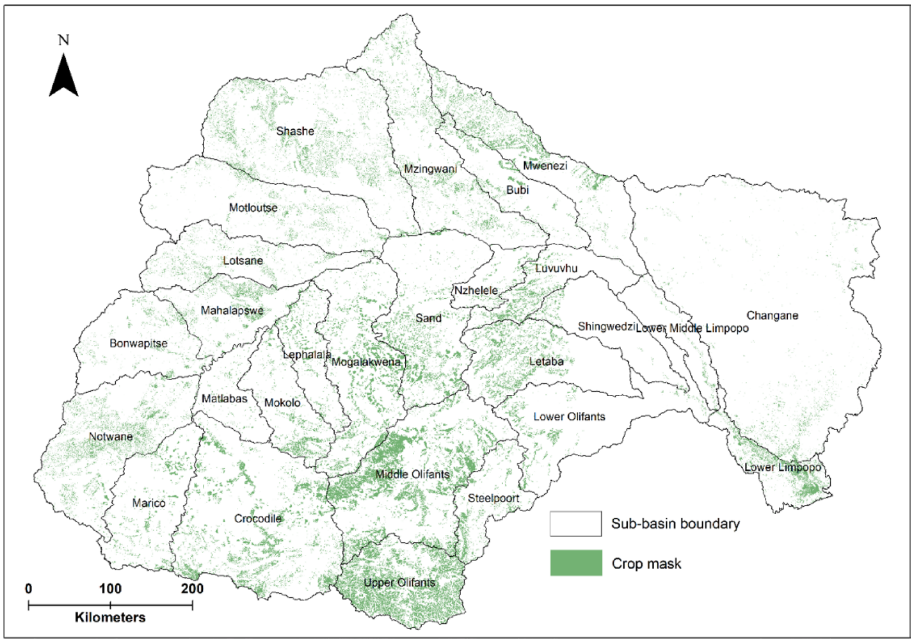

Fig. 8 Cropland mask of the Limpopo River Basin, derived from DALRRD cropland (2017) and SANLC (2022) for South Africa, and ESA WorldCover 10 m 2021 v200 for Botswana, Mozambique, and Zimbabwe

Cropland distribution varied substantially among sub-basins (Table 1). The Middle Olifants (659,301.6 ha) and Upper Olifants (582,542.6 ha) together contained over 28% of total cropland, followed by Crocodile (443,986.9 ha), Sand (269,569.4 ha), Shashe (247,169.2 ha), and Notwane (207,940.1 ha). In contrast, the Lower Middle Limpopo (12,529.1 ha), Matlabas (20,954.3 ha), and Shingwedzi (21,533 ha) had minimal coverage.

2.3.2 *Classification accuracy assessment*

Validation of the September 2024 irrigated-area map using 190 field reference points yielded an overall accuracy of 80% and a Cohen's Kappa (k) of 0.60 (Table 2). For the non-irrigated class, producer accuracy was 90.8% and user accuracy was 75.4%, with an F-score of 82.4%. The irrigated class achieved a producer accuracy of 68.5% and a user accuracy of 87.5% (F-score: 76.8%). The confusion matrix indicated that 89 of 98 non-irrigated samples and 63 of 92 irrigated samples were correctly classified. Misclassification was more common for irrigated plots, which were more often labelled as non-irrigated (29 cases), than for non-irrigated areas misclassified as irrigated (9 cases). Many errors occurred in fields at early phenological stages with high bare-soil fractions, producing spectral confusion with fallow or rainfed fields. McNemar's test confirmed a significant asymmetry in errors (χ^2 = 10.89, $p < 0.001$), indicating a conservative tendency to under-predict irrigated areas.

Values in the confusion matrix are shown as count (row %; % of total). Producer's accuracy corresponds to recall, user's accuracy to precision, and F-score to the class-wise F1 score.

Figure 9 shows model predictions of irrigated agriculture (highlighted in green) overlaid on true-color composites from PlanetScope imagery. Each pair of panels compares the original satellite view (left) with the corresponding classification output (right). The predictions capture a range of irrigation patterns, including irregularly shaped plots,

Table 1 Cropland extent by Limpopo sub-basin (ha). Cropland extent was derived from the study cropland mask used for irrigated-area mapping and summarized by sub-basin polygons for the Limpopo river basin

Sub-basin	Estimated cropland extent (ha)
Letaba	176,696.5
Lower Olifants	75,784.1
Sand	269,569.4
Mahalapswe	94,066.9
Matlabas	20,954.3
Nzhelele	26,690.8
Crocodile	443,986.9
Marico	95,785.3
Notwane	207,940.1
Bonwapitse	52,160.5
Mokolo	107,816.4
Lephalala	76,121.9
Mogalakwena	278,890.5
Motloutse	77,381.4
Shashe	247,169.2
Mzingwani	148,396.9
Bubi	58,425
Luvuvhu	87,327.4
Mwenezi	176,034.3
Upper Olifants	582,542.6
Middle Olifants	659,301.6
Steelpoort	96,457
Shingwedzi	21,533
Lower Middle Limpopo	12,529.1
Changane	75,594.5
Lower Limpopo	137,754.9
Lotsane	70,647.6

Table 2 Confusion matrix and accuracy metrics for September 2024 irrigated-area classification ($n = 190$) (a) confusion matrix

True\Predicted	Non-irrigated	Irrigated	Total
Non-irrigated	89 (90.8%; 46.8%)	9 (9.2%; 4.7%)	98 (100%; 51.6%)
Irrigated	29 (31.5%; 15.3%)	63 (68.5%; 33.2%)	92 (100%; 48.4%)
Total	118 (62.1%)	72 (37.9%)	190 (100%)
(b) Accuracy metrics			
Land class	Producer accuracy (%)	User accuracy (%)	F-score (%)
Non-irrigated	90.8	75.4	82.4
Irrigated	68.5	87.5	76.8
Overall/κ	Overall accuracy = 80.0		κ = 0.60

circular center-pivot systems, and rectangular fields, demonstrating the model's ability to identify irrigated areas across diverse field geometries and scales. In some cases, isolated pixels and boundary overestimation are visible, reflecting false positives associated with natural vegetation, bare soil, mixed pixels, or residual soil moisture in heterogeneous landscapes.

2.3.3 Temporal trends in irrigated area (2019–2024)

The monthly distribution of irrigated areas during the dry season (May–September) showed clear interannual variability (Fig. 10). Although 2019 recorded the highest

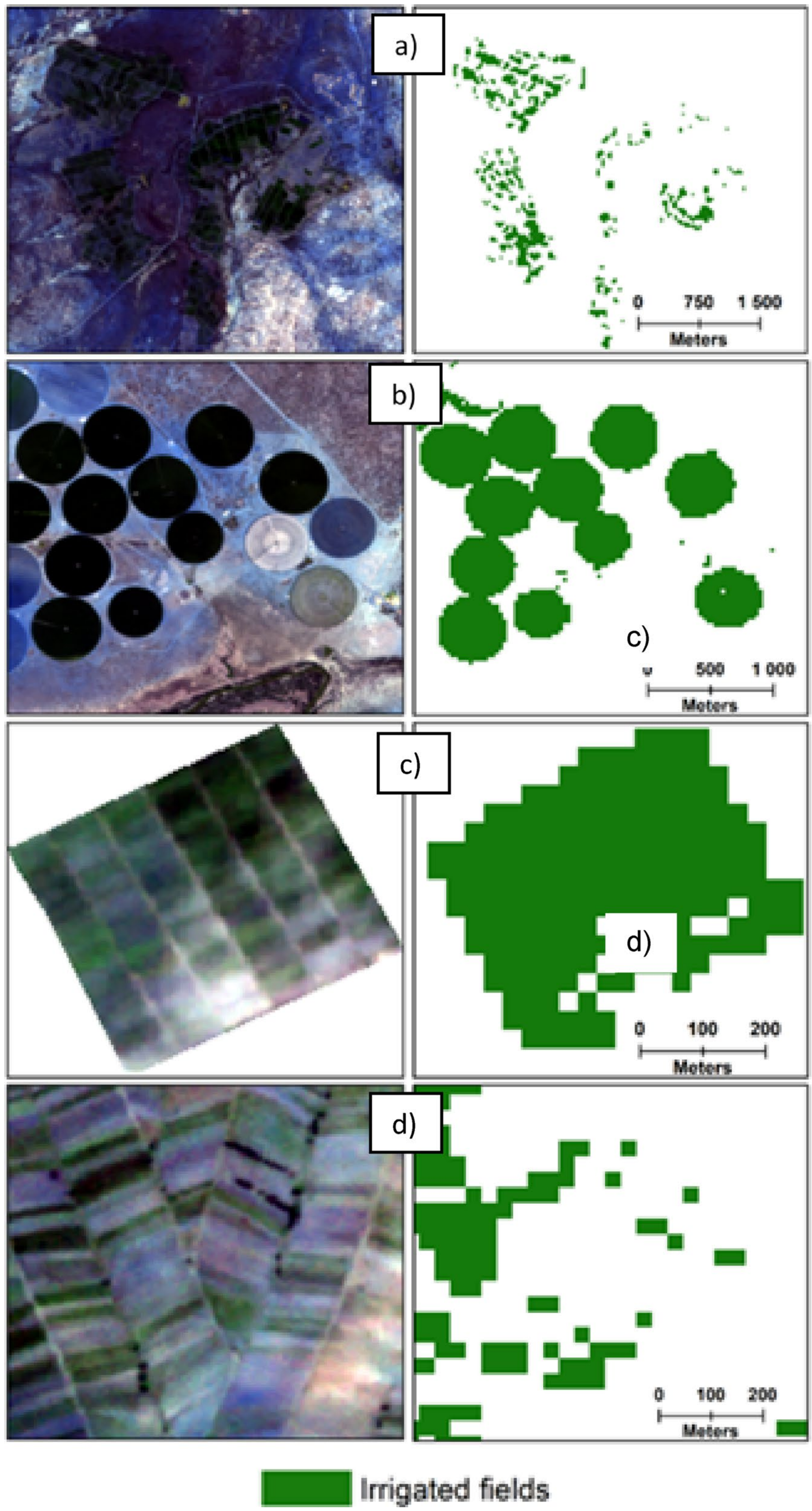

Fig. 9 (See legend on next page.)

(See figure on previous page.)
Fig. 9 Examples of irrigated areas derived from classification (right) alongside true-color PlanetScope composites (left, September 2024), provided through the Norwegian International Climate and Forest Initiative (NICFI). Panels illustrate (a) Silalabuhwa Irrigation Scheme, (b) a private commercial center-pivot irrigation farm on the Mahalapye River, (c) Zholube Irrigation Scheme, and (d) a smallholder irrigation scheme on the Mzingwane River in Matabeleland South, Zimbabwe. Correct detections show coherent field geometry and persistent dry-season greenness, while isolated pixels or boundary overestimation indicate false positives

seasonal mean irrigated area (~211,000 ha), interannual differences were modest. One-way ANOVA across years indicated no statistically significant differences ($F(5,24) = 0.84$, $p = 0.533$). The lowest seasonal mean occurred in 2020 (~171,113 ha), with July and August minima of ~112,435 ha and ~143,874 ha, respectively. In contrast, irrigated area differed significantly among months (one-way ANOVA across months: $F(4, 25) = 4.70$, $p = 0.00574$), and Tukey's HSD indicated that May was significantly higher than August ($p = 0.033$) and September ($p = 0.020$). From 2021 to 2023, seasonal means increased from ~175,386 ha to ~196,918 ha, while 2024 showed high early-season values (>210,000 ha) followed by lower late-season values. Linear regression of dry-season mean irrigated area for 2019–2024 indicated a weak downward trend. The trend was not statistically significant ($\beta = -1{,}341$ ha yr^{-1}, SE = 3,892, $t(4) = -0.35$, $p = 0.748$). Paired comparisons across years confirmed that May values were higher than August ($t(5) = 3.09$, $p = 0.027$) and September ($t(5) = 3.58$, $p = 0.0159$), consistent with continued cultivation following the preceding rainfed season.

2.3.4 Spatial distribution of irrigated area at the sub-basin level

Identified irrigated agriculture in the Middle Olifants, Crocodile, and Letaba sub-basins consistently accounted for the largest share of the Limpopo River Basin's irrigated area (Fig. 11). An exception occurred in September 2023, when irrigated area in the Crocodile sub-basin exceeded that of the Middle Olifants. In contrast, sub-basins such as Lotsane, Changane, Lower Middle Limpopo, Bubi, Bonwapitse, and Mahalapswe consistently exhibited lower irrigated area throughout 2019–2024.

Global Moran's I analysis revealed positive spatial autocorrelation of irrigated area across all years, indicating that irrigation is spatially clustered rather than randomly distributed among sub-basins. Using Queen contiguity weights, Moran's I ranged from 0.17 to 0.26, with statistically significant clustering observed in 2022 and 2023 ($p < 0.05$). A single spatial island (Steelpoort sub-basin) resulted in a disconnected contiguity graph. When a k-nearest neighbor ($k = 4$) spatial weights matrix was applied to ensure full connectivity, Moran's I values ranged from 0.15 to 0.20, with significant clustering detected particularly in 2019 and 2022. High-value clusters were concentrated in the central and northeastern parts of the basin, notably the Middle Olifants, Crocodile, and Letaba sub-basins. In contrast, lower irrigated area predominated in the western and southern sub-basins.

2.3.5 Progression of water consumption in irrigated agriculture (2019–2024)

Dry-season irrigation water consumption peaked in May and September, with a pronounced minimum in June (Fig. 12). The highest single-month value was recorded in May 2019 (189.8×10^6 m^3), while the lowest occurred in June 2020, indicating transition from rainfed to irrigated season (46.2×10^6 m^3). August consistently exhibited high and stable consumption across all years. Mean dry-season use increased from approximately

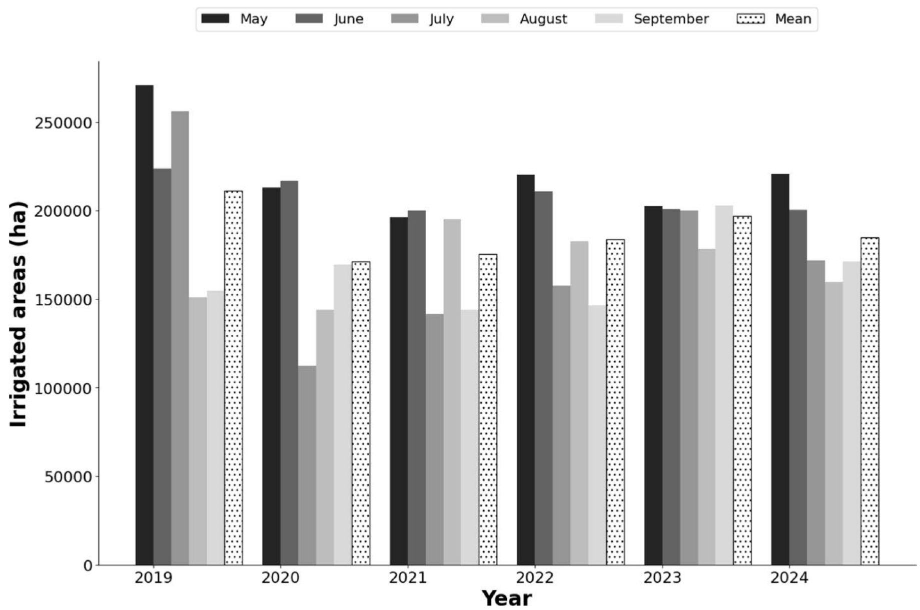

Fig. 10 Monthly irrigated area for the dry seasons from 2019 to 2024

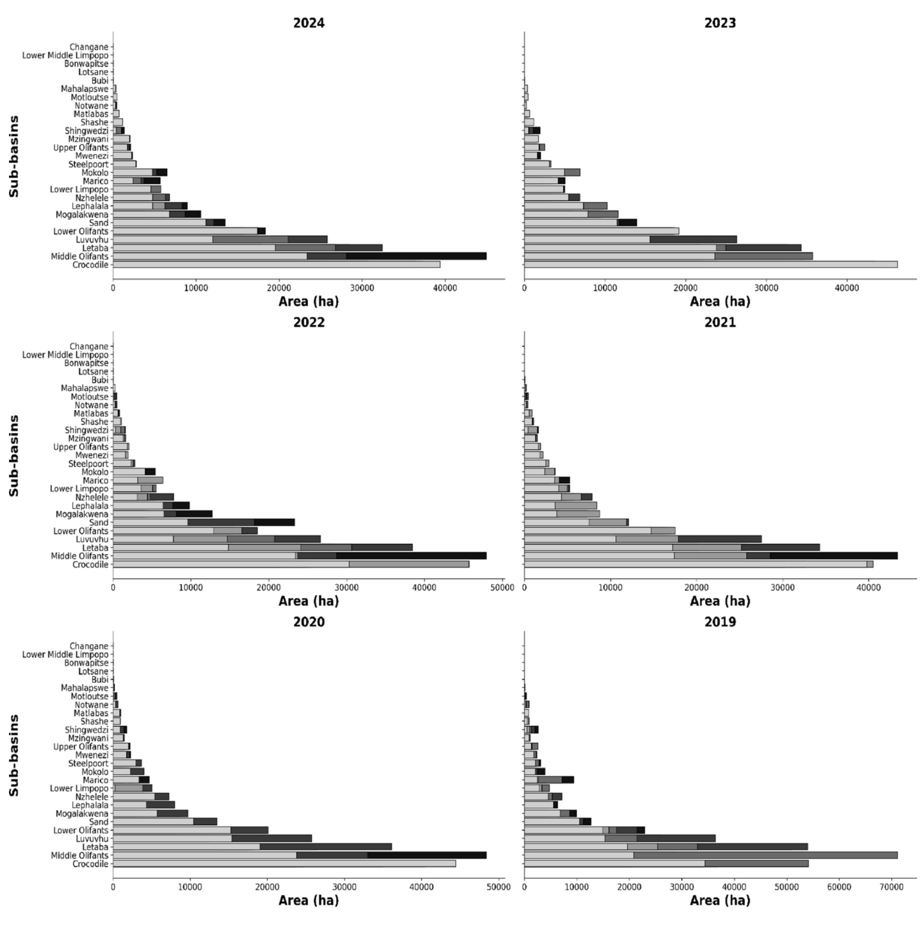

Fig. 11 Spatial distribution of irrigated areas across LRB sub-basins (2019–2024), highlighting concentration in Middle Olifants, Crocodile, Letaba, and Luvuvhu

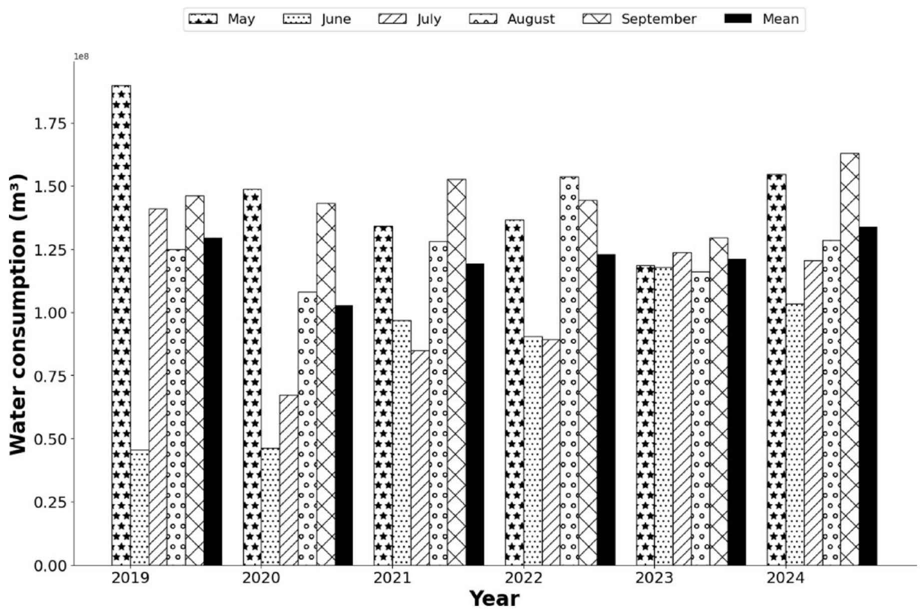

Fig. 12 Progression of water consumption of irrigated agriculture within LRB between 2019 and 2024

103×10^6 m^3 in 2020 to 134×10^6 m^3 in 2024. Across months, May had the highest mean consumption (147.4×10^6 m^3), whereas June recorded both the lowest mean (83.7×10^6 m^3) and the highest interannual variability (coefficient of variation, CV = 33.6%). A one-way ANOVA indicated significant differences among months ($F(4,25) = 8.54$, $p < 0.001$). Post-hoc Tukey's HSD revealed that August consumption was significantly higher than June (mean difference = 43.3×10^6 m^3, $p = 0.026$). These results confirm a strong seasonal pattern, with peaks at the start and end of the dry season, stable high usage in August, and a June minimum.

2.4 Discussion

2.4.1 Changes in irrigated area (2019–2024)

The results reveal an apparent decline in irrigated area over 2019–2024. However, interannual differences were not statistically significant. Similar irrigated-area estimates were reported by Cai et al. [5] and Van Niekerk et al. [41], who found 262,000 ha and 218,302 ha in Limpopo Province, respectively. These estimates were derived from coarser 30 m Landsat imagery and likely overestimated irrigated area due to mixed-pixel effects in heterogeneous agricultural landscapes [16, 17]. In contrast, the 10 m resolution of Sentinel-2 used in this study better resolves fragmented smallholder plots, which are a key feature of agricultural systems in the Limpopo River Basin (LRB).

The observed decline may reflect multiple interacting pressures. Increasing water stress is one possible factor. Kapangaziwiri et al. [18] documented a doubling of irrigation water consumption between 2000 and 2012 in already over-allocated sub-basins. The pronounced reduction in irrigated area observed in 2020 is temporally consistent with COVID-19 lockdowns across the basin, which disrupted agricultural operations and contributed to temporary farm abandonment [33]. Persistent drought conditions and water scarcity may also have constrained recovery in subsequent years. Water restrictions and reduced reservoir storage likely affected smallholder farmers most strongly [10, 24, 25, 29]. These drivers are plausible but were not explicitly tested in this study.

Spatially, irrigation remains clustered within a limited number of sub-basins that consistently account for the largest irrigated area. Global Moran's I shows significant positive spatial autocorrelation in most years ($I \approx 0.16$–0.26), confirming that irrigated agriculture in the basin is spatially clustered rather than randomly distributed. In contrast, several sub-basins consistently exhibit minimal irrigation. While these patterns identify persistent irrigation hotspots, this study does not quantify the hydrological, infrastructural, or institutional drivers behind them.

At the intra-annual scale, irrigated area is higher during the early dry season (May–June) and declines during later months (August–September). These differences reflect seasonal adjustments in irrigation activity as water availability decreases through the dry season [26]. Smallholder farmers often face constraints related to pumping costs and limited storage and may therefore reduce irrigation later in the season or revert to rainfed practices, increasing vulnerability to drought [30].

2.4.2 Water use dynamics

Irrigation water consumption shows a strong seasonal pattern. Water use peaks in May (147.4×10^6 m^3) and September. The lowest values occur in June (83.7×10^6 m^3; CV = 33.6%) (Fig. 12). These patterns are consistent with the dry-season dynamics of the LRB. They can be interpreted in relation to regional cropping calendars. Late autumn (May) often coincides with the end of summer cropping and the transition to winter irrigated production. Winter wheat is commonly planted in June–July. During this stage, crop water requirements are relatively low [1, 21, 38]. By early spring (September), crop establishment and rising atmospheric demand increase irrigation requirements before the onset of consistent rainfall [2, 6]. This seasonal context is important for interpreting longer-term changes in irrigation water use independently of irrigated area extent.

Mean dry-season water use increased from approximately 103×10^6 m^3 in 2020 to about 134×10^6 m^3 in 2024. This occurred despite relatively stable interannual irrigated area. The pattern suggests an increase in irrigation intensity, expressed as water use per unit irrigated area. This indicates intensification rather than spatial expansion of irrigation. This may reflect greater reliance on irrigation during drier conditions. Changes in scheme operation or water sourcing may also play a role [2, 21]. Other explanations cannot be excluded. These include shifts toward more water-intensive crops, changes in irrigation efficiency, or conservative classification that retains only strongly irrigated fields. Such intensification has important implications for basin water security, particularly in already water-stressed and over-allocated sub-basins. The available analysis does not allow these mechanisms to be separated.

The low water-use values observed in 2020 are consistent with COVID-19–related disruptions to agricultural activity [33]. However, this association should not be interpreted as a definitive causal relationship. The non-significant interannual trend in irrigated area supports a cautious interpretation focused on water-use intensity rather than land-use change.

2.4.3 Strengths and limitations

The framework demonstrates strong operational potential by combining automation, scalability, and high spatial resolution. Leveraging Google Earth Engine enables basin-wide monthly mapping without reliance on continuous in-season field data. Post-classification refinements, such as time-lagged precipitation–vegetation filtering and slope masking, reduce misclassification from perennial vegetation and topographically implausible irrigation. The integration of WaPOR evapotranspiration data links mapped irrigated area with actual water use. This strengthens the framework's relevance for basin-scale water allocation and planning. Irrigation water use is estimated as the product of irrigated area and evapotranspiration. Uncertainty in both components therefore affects volumetric water-use estimates.

Validation against independent field observations yielded an overall accuracy of approximately 80% ($\kappa \approx 0.60$). This level of agreement is appropriate for basin-scale operational monitoring. Error analysis reveals an asymmetric misclassification pattern. Irrigated fields are more often under-predicted than overestimated. This conservative bias is strongest during early phenological stages, when bare soil reduces spectral separability. It is further reinforced by strict post-classification filtering. This approach reduces false identification of rainfed or perennial systems as irrigated. This is advantageous in water-scarce basins, where overestimation could lead to inappropriate water allocation decisions. However, it may omit marginal or early-season irrigation activity. As a result, mapped irrigated area and associated water-use estimates may be conservative where irrigation signals are weak or transient. Omission errors therefore directly reduce estimated irrigation water use. Reported water-use values should be interpreted as lower-bound estimates, particularly in allocation and demand-assessment contexts.

Several limitations should be considered when interpreting the results. First, in-situ validation was concentrated in South Africa's Limpopo Province due to logistical constraints. This may limit transferability of reported accuracy metrics to other parts of the basin. Differences are expected in Botswana and Mozambique, where cropping systems, field sizes, and irrigation practices vary. Supplementary validation using high-resolution imagery and known irrigation scheme locations partially mitigates this limitation. Expanded field validation across additional basin countries remains a priority for future work.

The use of a static cropland mask does not explicitly account for cropland expansion or abandonment during the study period. In rapidly changing agricultural zones, this may result in omission of newly cultivated fields or retention of areas that have transitioned out of crop production. These effects may influence local estimates but are expected to diminish when irrigated area and water use are aggregated to sub-basin or basin scale, which is the primary focus of this study.

Second, WaPOR AETI was resampled from its native 100 m resolution to 10 m using nearest-neighbour interpolation. This preserves original pixel values. However, it can introduce spatial artifacts at field boundaries and within mixed pixels. These effects are most pronounced in fragmented smallholder landscapes. They are expected to diminish when results are aggregated to sub-basin or basin scale. At fine spatial scales, they introduce uncertainty in attributing evapotranspiration to irrigated areas. This uncertainty is independent of classification performance.

Uncertainty in volumetric irrigation water-use estimates arises from both classification error and uncertainty in WaPOR AETI. Total water use is calculated as the product of irrigated area and evapotranspiration. Uncertainty therefore propagates multiplicatively. This results in a range of plausible values rather than a single deterministic estimate. At basin scale, some local errors may offset each other. Systematic under-prediction of irrigated area, however, propagates directly into aggregated water-use totals. In this study, water-use estimates are reported as point values. This supports operational clarity and near-real-time decision-making. Point estimates are sufficient for comparing spatial patterns and temporal trends, but they should be interpreted conservatively for allocation purposes. Future work will explicitly propagate uncertainty. This will combine classification confidence, validation-derived error rates, and alternative AETI aggregation methods to derive uncertainty bounds.

Finally, post-classification refinements reduce commission errors. Perennial tree crops remain a potential source of localized misclassification. Persistent greenness does not always indicate irrigation timing. The semi-supervised approach reduces dependence on costly field surveys. Some level of ground-based validation remains essential. This is needed to benchmark performance and adapt the framework to new agro-ecological contexts.

2.4.4 Implications and future directions

The high-resolution, monthly irrigated area maps and associated water use estimates produced by this framework provide an evidence base that was previously unavailable for the LRB. By linking spatially explicit irrigated area with water consumption, the system enables monitoring of irrigation dynamics throughout the dry season, including identification of peaks in water use and shifts in cultivation patterns over time.

The capacity to capture smallholder fields at 10 m resolution is particularly valuable. These plots are often underrepresented in coarser-scale assessments, yet they play a central role in household food security and rural livelihoods. By including both smallholder and commercial irrigation in the same monitoring system, the methodology provides a more complete picture of agricultural water use.

At the same time, the spatial distribution maps highlight irrigation hotspots, such as the Middle Olifants and Crocodile sub-basins, where water use is concentrated. Basin agencies can operationalize these outputs by using the monthly dry-season cadence to implement alert-based monitoring that flags statistically meaningful increases in irrigated area or water use (reported with uncertainty bounds), with predefined thresholds triggering follow-up verification or targeted management actions. Future work should evaluate how these mapped hotspots relate to hydrological availability, infrastructure, and governance variables through targeted, basin-wide analyses. The detection of underutilized areas may indicate potential for agricultural expansion, but this would require hydrological assessment to confirm that water resources are available [34]. In the longer term, embedding this monitoring system within the Limpopo Digital Twin initiative could support operational dissemination and reproducibility, provided that outputs are communicated with appropriate uncertainty information and validation across basin countries is expanded.

2.5 Conclusions

This study developed and validated a scalable, high-resolution, semi-supervised machine learning framework for monthly mapping of irrigated area and associated water use in the LRB from 2019 to 2024, addressing a critical need for precise irrigation monitoring in a water-stressed transboundary region. By integrating Sentinel-2 imagery, Random Forest classification, time-lagged precipitation–vegetation relationships, slope-based masking, and FAO's WaPOR evapotranspiration data, the framework achieved an overall accuracy of 80% (Cohen's Kappa = 0.60), effectively capturing smallholder plots and monthly dynamics at a 10 m resolution. The findings reveal a downward trend in irrigated areas, from ~211,281 ha in 2019 to ~184,771 ha in 2024, alongside an increase in dry-season water use from 103×10^6 m^3 in 2020 to 134×10^6 m^3 in 2024, highlighting intensifying water stress and the impact of factors such as drought and COVID-19 disruptions. Spatial concentration in the Middle Olifants, Crocodile, Letaba, and Luvuvhu sub-basins underscores the need for targeted water management, while underutilized sub-basins present opportunities for sustainable irrigation expansion. Despite limitations, such as misclassification at early crop stages, the framework provides actionable insights for equitable water allocation and agricultural planning. Future enhancements, including expanded validation and additional data sources, could further strengthen its applicability across other water-stressed basins, positioning it as a vital tool for sustainable water resource management in climatically vulnerable regions.

Supplementary Information

The online version contains supplementary material available at https://doi.org/10.1007/s43832-026-00360-z.

Supplementary Material 1

Author contributions

Zolo Kiala : conceptualization, methodology, data curation, formal analysis, software development, visualization, writing – original draft. Karthikeyan Matheswaran : supervision, methodological guidance, validation, writing. Chris Dickens : interpretation of results, writing. Mariangel Garcia Andarcia : modelling, funding acquisition. Fulco Ludwig : Supervision, writing. Surajit Ghosh : methodological guidance, writing.

Funding

This research was funded by CGIAR through the CGIAR Initiative on Digital Innovation, supported by CGIAR Trust Fund contributors.

Data availability

The irrigated-area mapping workflow was implemented in Google Earth Engine (GEE). To support reproducibility, we provide (i) the end-to-end GEE script used to generate monthly dry-season irrigated-area products, and (ii) a separate GEE script that reproduces the semi-supervised reference-data generation based on NGI percentiles.- Full GEE workflow (monthly mapping + post-classification refinement + export): [https://shorturl.at/GYUn1](https:/shorturl.at/GYUn1)- Reference-data generation workflow (NGI percentile sampling): [https://code.earthengine.google.com/a97003607b4ae118e717b5faa66bb73d](https:/code.earthengine.google.com/a97003607b4ae118e717b5faa66bb73d)All statistical analyses (ANOVA, Tukey HSD, paired t-tests, McNemar's test, Moran's I) were performed in Python, and the executable notebook is available at:- Python analysis notebook: [https://colab.research.google.com/drive/1cQXLsPBT1RDSBtuFEXgdSl4sz56fWL7H? usp=sharing](https:/colab.research.google.com/drive/1cQXLsPBT1RDSBtuFEXgdSl4sz56fWL7H?usp=sharing)2. Access to Derived ProductsThe derived monthly dry-season irrigated-area maps (10 m), irrigated-area probability layers, and basin/sub-basin summary tables for 2019–2024 are available as open products through the Limpopo Basin Digital Twin initiative:- Portal access: [https://limpopo.digitaltwins.iwmi.org/](https:/limpopo.digitaltwins.iwmi.org)In addition, an interactive implementation that enables replication and adaptation to other basins is available at:- Interactive application: [https://huggingface.co/spaces/IWMIHQ/irrigated-agriculture-extractor](https:/huggingface.co/spaces/IWMIHQ/irrigated-agriculture-extractor)For transparency and reuse, the derived layers used in the analysis are also available as Google Earth Engine (GEE) assets (paths listed in the Supplementary Table), including known irrigation scheme boundaries, surveyed irrigated field locations, and basin/sub-basin polygons (e.g., projects/tethys-app-1/assets/known_irr_schemes, projects/tethys-app-1/assets/surveyed_irrigated_fields, projects/tethys-app-1/assets/lrb_subbasin). In addition, a Google Colab notebook for visualizing and downloading the derived datasets is publicly available at: [https://shorturl.at/OmAcl](https:/shorturl.at/OmAcl) .

Declarations

Ethical approval
Not applicable.

Consent to participate
Not applicable.

Consent to publish
Not applicable.

Clinical trial number
Not applicable.

Competing interests
The authors declare no competing interests.

Received: 16 October 2025 / Accepted: 2 February 2026
Published online: 14 February 2026

References

1. Al-Kaisi MM, Broner I. Crop water use and growth stages. USA: Colorado State University Extension Fort Collins, CO; 2009.
2. Botai CM, Botai JO, Zwane NN, Hayombe P, Wamiti EK, Makgoale T, Murambadoro MD, Adeola AM, Ncongwane KP, de Wit JP, Mengistu MG, Tazvinga H. (2020) Hydroclimatic extremes in the Limpopo.
3. Box GEP, Jenkins GM, Reinsel GC, Ljung GM. Time series analysis: forecasting and control. 5th ed. Hoboken: Wiley; 2015.
4. Breiman L. Random forests. Mach Learn. 2001;45:5–32. https://doi.org/10.1023/A:1010933404324.
5. Cai X, Magidi J, Nhamo L, Van Koppen B. Mapping irrigated areas in the Limpopo Province, South Africa. International Water Management Institute (IWMI); 2017.
6. Chadalavada K, Kumari BR, Kumar TS. (2021) Sorghum mitigates climate variability and change on crop yield.
7. Chukalla AD, Mul ML, van der Zaag P, van Halsema G, Mubaya E, Muchanga E, den Besten N, Karimi P. A framework for irrigation performance assessment using WaPOR data: the case of a sugarcane estate in Mozambique. Hydrol Earth Syst Sci. 2022;26:5087–102. https://doi.org/10.5194/hess-26-5087-2022.
8. Dickens C, Mukuyu P, Ndlovu B, O'Brien G, Stassen R, Magombeyi M, United States Agency for International Development (USAID). (2020) E-flows for the Limpopo River Basin: from vision to management. Project report prepared by the International Water Management Institute (IWMI) for the. Colombo, Sri Lanka: International Water Management Institute (IWMI); Washington, DC, USA: USAID. 104p. (E-flows for the Limpopo River Basin: Report 3). https://doi.org/10.5337/2022.218
9. FAO. WaPOR database methodology: level 3 data – Using remote sensing in support of solutions to reduce agricultural water productivity gaps. Rome: Food and Agriculture Organization of the United Nations; 2019. p. 68.
10. Ferreira KR, Queiroz GR, Marujo RFB, Costa RW. Building Earth observation data cubes on Aws. Int Arch Photogramm Remote Sens Spat Inf Sci. 2022;XLIII–B3–2022:597–602. https://doi.org/10.5194/isprs-archives-XLIII-B3-2022-597-2022.
11. Franceschini G, Khan A, Moretti L, Nyabuti K, Asif M, Bezuidenhoudt E, Morteo K. The global administrative unit layers (GAUL) 2024. Technical guidelines. Rome: Food and Agriculture Organization of the United Nations; 2025. https://doi.org/10.4060/cd4262en.
12. Funk C, Peterson P, Landsfeld M, Pedreros D, Verdin J, Shukla S, Husak G, Rowland J, Harrison L, Hoell A, Michaelsen J. The climate hazards infrared precipitation with stations—a new environmental record for monitoring extremes. Sci Data. 2015;2:150066. https://doi.org/10.1038/sdata.2015.66.
13. Gao B-C. NDWI—A normalized difference water index for remote sensing of vegetation liquid water from space. Remote Sens Environ. 1996;58:257–66. https://doi.org/10.1016/S0034-4257(96)00067-3.
14. Glenn EP, Huete AR, Nagler PL, Nelson SG. Relationship between remotely sensed vegetation indices, canopy attributes and plant physiological processes: what vegetation indices can and cannot tell Us about the landscape. Sensors. 2008;8:2136–60. https://doi.org/10.3390/s8042136.
15. Gorelick N, Hancher M, Dixon M, Ilyushchenko S, Thau D, Moore R. Google Earth engine: Planetary-scale Geospatial analysis for everyone. Remote Sens Environ. 2017;202:18–27. https://doi.org/10.1016/j.rse.2017.06.031.
16. Gxokwe S, Dube T, Mazvimavi D. Leveraging Google Earth engine platform to characterize and map small seasonal wetlands in the semi-arid environments of South Africa. Sci Total Environ. 2022;803:150139. https://doi.org/10.1016/j.scitotenv.2021.150139.
17. He Y, Yang J, Guo X. Green vegetation cover dynamics in a heterogeneous grassland: spectral unmixing of Landsat time series from 1999 to 2014. Remote Sens. 2020;12:3826. https://doi.org/10.3390/rs12223826.
18. Kapangaziwiri E, Mwenge Kahinda J-M, Oosthuizen N, Mvandaba V, Hobbs P, Hughes DA. Towards the quantification of the historical and future water resources of the Limpopo river basin. Pretoria, South Africa: Water Research Commission; 2021.
19. Lehner B, Verdin K, Jarvis A. New global hydrography derived from spaceborne elevation data. Eos Trans Am Geophys Union. 2008;89:93–4. https://doi.org/10.1029/2008EO100001.
20. Lillesand T, Kiefer RW, Chipman J. Remote sensing and image interpretation. 7th ed. Hoboken: Wiley; 2015.
21. Limpopo Basin Permanent Technical Committee. (2010) Joint Limpopo River Basin Study Scoping Phase Final Report. Limpopo Basin Permanent Technical Committee, Maputo, Mozambique. Available at: https://dsc.duq.edu/limpopo-reports/1.
22. Magidi J, Nhamo L, Mpandeli S, Mabhaudhi T. Application of the random forest classifier to map irrigated areas using Google Earth engine. Remote Sens. 2021;13:876. https://doi.org/10.3390/rs13050876.
23. Mahapatra S, Velpuri N, Schmitter P, Pandey S, Sikka A. (2024) Enhancing the water accounting plus framework to evaluate field-level water use and availability in rice-dominant cropping system and potential for mapping GHG emissions at scale:

a case study for the eastern Gangetic Plains, Bihar, India. International Water Management Institute (IWMI), Colombo, Sri Lanka. Available at: https://cgspace.cgiar.org/items/02a516b8-60d5-4a12-97 cc-87e1518307da.
24. Makhanya NZ. (2021) Potential impacts of climate change on hydrological droughts in the Limpopo river basin. Master's thesis, University of Cape Town, Cape Town, South Africa. Available at: https://open.uct.ac.za/items/ef087102-2c7d-4460-8415-d04087012ee5.
25. Mathivha FI, Mabala L, Matimolane S, Mbatha N. El Niño-Induced drought impacts on reservoir water resources in South Africa. Atmosphere. 2024;15:249. https://doi.org/10.3390/atmos15030249.
26. Mazibuko SM, Mukwada G, Moeletsi ME. Assessing the frequency of drought/flood severity in the Luvuvhu river catchment, Limpopo Province, South Africa. Water SA. 2021;47:172–84. https://doi.org/10.17159/wsa/2021.v47.i2.10913.
27. McAllister A, Whitfield D, Abuzar M. Mapping irrigated farmlands using vegetation and thermal thresholds derived from Landsat and ASTER data in an irrigation district of Australia. Photogramm Eng Remote Sens. 2015;81:229–38. https://doi.org/10.14358/PERS.81.3.229.
28. Mpakairi KS, Dube T, Sibanda M, Mutanga O. Fine-scale characterization of irrigated and rainfed croplands at National scale using multi-source data, random forest, and deep learning algorithms. ISPRS J Photogramm Remote Sens. 2023;204:117–30. https://doi.org/10.1016/j.isprsjprs.2023.09.006.
29. Mukwevho SG. (2023) Modelling impacts of climate change on hydrology of Latonyanda River Quaternary Catchment, Limpopo Province, South Africa. Master's dissertation, University of Venda, Thohoyandou, South Africa. Available at: https://univendspace.univen.ac.za/items/3a40197b-ef4f-493e-8811-f59f90d8b94a.
30. Olabanji MF, Davis N, Ndarana T, Kuhudzai AG, Mahlobo D. Assessment of smallholder farmers' perception and adaptation response to climate change in the olifants catchment, South Africa. J Water Clim Change. 2021;12:3388–403. https://doi.org/10.2166/wcc.2021.138.
31. Ozdogan M, Gutman G. A new methodology to map irrigated areas using multi-temporal MODIS and ancillary data: an application example in the continental US. Remote Sens Environ. 2008;112:3520–37. https://doi.org/10.1016/j.rse.2008.04.010.
32. Ozdogan M, Yang Y, Allez G, Cervantes C. Remote sensing of irrigated agriculture: opportunities and challenges. Remote Sens. 2010;2:2274–304. https://doi.org/10.3390/rs2092274.
33. Paganini N, Adinata K, Buthelezi N, Harris D, Lemke S, Luis A, Koppelin J, Karriem A, Ncube F, Nervi Aguirre E, Ramba T, Raimundo I, Sulejmanović N, Swanby H, Tevera D, Stöber S. Growing and eating food during the COVID-19 pandemic: farmers' perspectives on local food system resilience to shocks in Southern Africa and Indonesia. Sustainability. 2020;12:8556. https://doi.org/10.3390/su12208556.
34. Perrin J, Ferrant S, Massuel S, Dewandel B, Maréchal JC, Aulong S, Ahmed S. Assessing water availability in a semi-arid watershed of Southern India using a semi-distributed model. J Hydrol. 2012;460–461:143–55. https://doi.org/10.1016/j.jhydrol.2012.07.002.
35. Pun M, Mutiibwa D, Li R. Land use classification: A surface energy balance and vegetation index application to map and monitor irrigated lands. Remote Sens. 2017;9:1256. https://doi.org/10.3390/rs9121256.
36. Ragettli S, Herberz T, Siegfried T. An unsupervised classification algorithm for Multi-Temporal irrigated area mapping in central Asia. Remote Sens. 2018;10:1823. https://doi.org/10.3390/rs10111823.
37. Senay GB, Friedrichs M, Singh RK, Velpuri NM. Evaluating Landsat 8 evapotranspiration for water use mapping in the Colorado river basin. Remote Sens Environ. 2016;185:171–85. https://doi.org/10.1016/j.rse.2015.12.043.
38. Sihlobo W. (2022) What the month of April means for SA agriculture. Agricultural Business Chamber of South Africa (Agbiz), Pretoria, South Africa. Available at: https://www.agbiz.co.za/document/open/what-the-month-of-april-means-for-sa-agriculture.
39. Sitoe S, Qwist-Hoffman P. (2013) Limpopo River Basin Monograph. Limpopo Watercourse Commission (LIMCOM), Maputo, Mozambique. Available at: https://dsc.duq.edu/limpopo-policy/1.
40. Thenkabail PS, Biradar CM, Noojipady P, Dheeravath V, Li Y, Velpuri M, Gumma MK, Gangalakunta ORP, Turral H, Cai X, Vithanage J, Schull MA, Dutta R. Global irrigated area map (GIAM), derived from remote sensing, for the end of the last millennium. Int J Remote Sens. 2009;30:3679–733. https://doi.org/10.1080/01431160802698919.
41. Van Niekerk A, Jarmain C, Goudriaan R. (2018) An earth observation approach towards mapping irrigated area and quantifying water use by irrigated crops in South Africa. Water Research Commission, Pretoria, South Africa. Report No. TT 745/17. Available at: https://www.wrc.org.za/wp-content/uploads/mdocs/TT%20745%20Final%20Report%20reprint%2025%2005%2018.pdf.
42. Vogels MF, de Jong SM, Sterk G, Addink EA. Mapping irrigated agriculture in complex landscapes using SPOT6 imagery and object-based image analysis–A case study in the central rift Valley, Ethiopia–. Int J Appl Earth Obs Geoinf. 2019;75:118–29. https://doi.org/10.1016/j.jag.2018.07.019.
43. Zanaga D, Van De Kerchove R, Daems D, De Keersmaecker W, Brockmann C, Kirches G, Wevers J, Cartus O, Santoro M, Fritz S, Lesiv M, Herold M, Tsendbazar N-E, Xu P, Ramoino F, Arino O. (2022) ESA WorldCover 10 m 2021 v200. European Space Agency, Paris, France. https://doi.org/10.5281/zenodo.7254221.
44. Zhang X, Liu L, Chen X, Xie S, Gao Y. Fine land-cover mapping in China using Landsat datacube and an operational SPECLib-based approach. Remote Sens. 2019;11:1056. https://doi.org/10.3390/rs11091056.
45. Zurqani HA, Allen JS, Post CJ, Mikhailova EA, Lalk S. Mapping and quantifying agricultural irrigation in heterogeneous landscapes using Google Earth engine. Remote Sens Appl Soc Environ. 2021;23:100590. https://doi.org/10.1016/j.rsase.2021.100590.